In-situ birefringence microscopy of uniaxially stretched metal-polymer laminate

van Tijum, R.; de Jong, B. V. C.; Vellinga, W. P.; De Hosson, J. Th. M.

Published in:
Surface & Coatings Technology

DOI:
10.1016/j.surfcoat.2006.10.002

Publication date:
2007

Available online at www.sciencedirect.com
ScienceDirect
Surface & Coatings Technology 201 (2007) 4633–4639
SURFACE & COATINGS TECHNOLOGY
www.elsevier.com/locate/surfcoat

In-situ birefringence microscopy of uniaxially stretched metal–polymer laminate

R. van Tijum, B.V.C. de Jong, W.P. Vellinga, J.Th.M. De Hosson *

Department of Applied Physics, Materials Science Centre and the Netherlands Institute for Metals Research, University of Groningen, Nijenborgh 4, 9747 AG Groningen, The Netherlands

Received 28 July 2006; accepted in revised form 2 October 2006
Available online 27 November 2006

Abstract

This paper concentrates on revealing the local deformation as a function of applied strain in a polymer coating supported by a plastically deforming and roughening metal substrate. To this end in-situ birefringence microscopy measurements have been executed. The measurements are performed in reflection and an alternative unwrapping scheme for the optical path difference is proposed. From the characterization of PET (polyethylene terephthalate) coated stainless steel it is concluded that strain localization appears below the macroscopic strain at yield and that the surface roughness of the substrate is the driving force of the localization.

Keywords: Metal–polymer coating; In-situ birefiringence microscopy; Shear bands; Interface roughness

1. Introduction

Polymer-coated steels are commonly used in the packaging industry to protect the content of the can from the steel and vice versa. During the forming process, the coating should remain functionally in tact, i.e. it should fully adhere to the steel. An important issue during deformation of polymer-coated steels is the induced roughening of the steel substrate [1,2]. Effects of roughening on the adhesion at the interface between an amorphous polymer and steel were studied in Refs. [3–5]. Using polarization microscopy it was shown qualitatively that microscopic phenomena of deformation at a certain global strain of the thin layer of amorphous polymer differ considerably from what is expected in the bulk [5]. As soon as the steel substrate deforms plastically, stress concentrations occur in the amorphous polymer layer near the interface that lead to localized shear bands. These shear bands already occur at strains below the yield strain of the bulk PET (polyethylene terephthalate). This behavior near the interface continues at higher stresses. Above the yield strain of PET, the deformation of the film is highly inhomogeneous with patterns of shear bands at 45 degrees with respect to the loading direction. Localized necking perpendicular to the tensile direction occurs only for very thick samples [6,7].

Calculations performed in Ref. [5] show the evolution of the deformation in the layer, which is in qualitative agreement with experiments. Moreover, in these calculations it appears that although the energy release rate G decreases monotonically as a function of strain, the stresses acting at the interface drop if the global strain surpasses the yield strain of the amorphous polymer. It is expected that the stresses acting at the interface affect the rate at which various thermally activated degradation mechanisms (delamination, corrosion) occur [8]. Potentially a decrease in stress level near an interface (even though it occurs at a higher deformation) might be favorable in terms of the lifetime of the interface. Therefore, it is relevant to measure the stresses acting in the polymer layer as a function of global strain. Recent theoretical advances have shown that full-field microscopic measurements of the birefringence can be executed after relatively small modifications to existing optical (transmission) microscopes are made [9,10]. Since the birefringence is related to the state of strain in the layer, such measurements therefore offer in principle the possibility to relate strains and stresses in the deformed polymer layer to the adhesion or delamination behavior.

* Corresponding author.
E-mail address: j.t.m.de.hosson@rug.nl (J.Th.M. De Hosson).

0257-8972/$ - see front matter © 2006 Elsevier B.V. All rights reserved.
doi:10.1016/j.surfcoat.2006.10.002

This paper concentrates on in-situ birefringence measurements to quantify the differences in strain that occur in polymer layers deformed together with a steel substrate. The experimental technique and the interpretation of the results are very similar to the ones described in Refs. [9,10] but differs in two ways: the measurements are performed in reflection, and an alternative unwrapping scheme for the optical path difference is proposed. These differences will be discussed.

2. Theoretical background

Polarization microscopy is a well-known technique for studying birefringent transparent materials under stress [10]. Birefringence Δn may be defined as $\Delta n = n_{\parallel} - n_{\perp}$, where $n_{\parallel}$ and $n_{\perp}$ are the refractive indices parallel and perpendicular to the local principal strain direction, respectively [11]. For an amorphous polymer Δn can be expressed as a function of the orientation order parameter $\langle f \rangle$ [12]:

$$\Delta n = \Delta n_{\max} \langle f \rangle. \tag{1}$$

When monomers are randomly distributed in space (in amorphous and unstretched state) $\langle f \rangle = 0$. Due to straining the chains will orient and $\Delta n_{\max}$ will be attained when $\langle f \rangle = 1$.

Two models have been proposed for predicting $\langle f \rangle$ as a function of strain ε, i.e. affine and pseudo-affine models [13,14]. In the affine model flexible chains connect a network of fixed junctions. When the network is stretched it is assumed that all local deformations are proportional to the macroscopic deformations. In this case the orientation order parameter can be expressed as:

$$\langle f \rangle = \frac{1}{5N}\left(\lambda^2 - \lambda^{-1}\right) \overset{\varepsilon \to 0}{\approx} \frac{3\varepsilon}{5N}, \tag{2}$$

where N is the number of random links between network points, $\lambda = \varepsilon + 1$ is the draw-ratio and ε is the strain. The pseudo-affine model assumes that the structural elements are rigid. These elements are able to rotate in order to accommodate the deformation. In this case $\langle f \rangle$ can be expressed as [14]:

$$\langle f \rangle = \frac{1}{2}\left(\frac{2\lambda^3 + 1}{\lambda^3 - 1} - \frac{3\lambda^3}{(\lambda^3 - 1)^{3/2}} \tan^{-1}\sqrt{\lambda^3 - 1}\right) \overset{\varepsilon \to 0}{\approx} \frac{3\varepsilon}{5}. \tag{3}$$

In both cases at small strains Δn is linear with deformation. In fact, only the principle strain difference occurs in Δn:

$$\Delta n = \Delta n_{\max} \langle f(\varepsilon) \rangle = S_{\text{opt}}(\varepsilon_2 - \varepsilon_1), \tag{4}$$

where S_{opt} is a constant and ε_1 and ε_2 are the principal strains. It has been found that below the glass transition temperature T_g pseudo-affine models show a good agreement with experiments. For an amorphous polymer above T_g, $\langle f \rangle$ shows the same dependence on λ as the stress if one assumes affine deformation. As a consequence the well-known stress-optical rule is valid at all strains [12] and reads:

$$\Delta n = C_{\text{opt}}(\sigma_2 - \sigma_1), \tag{5}$$

where C_{opt} is the stress-optical coefficient. In general, below T_g Eq. (5) is only valid in the elastic regime.

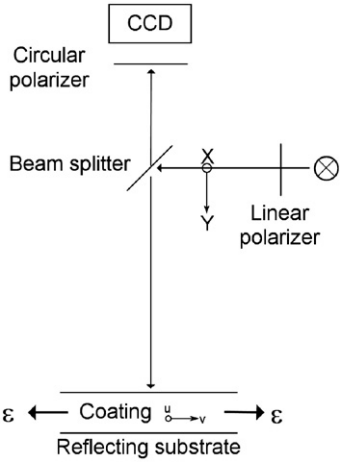

Fig. 1. Schematic picture of the birefringence microscope.

Δn can be measured by establishing the so-called phase factor δ:

$$\delta = \frac{2\pi L(\varepsilon)\Delta n}{\lambda}, \tag{6}$$

where λ is the wavelength of the radiation, $L(\varepsilon) = L_0(1 - \nu\varepsilon)$ is the thickness of the sample at a strain ε and ν is the Poisson's ratio of the coating. For full field birefringence microscopy a number of methods have recently been proposed in which a sample is illuminated with a rotating linear polarizer, and in which a circular polarizer is used as analyzer [9,11].

The relation between the $\vec{E}$–field of the exiting and illuminating radiation can be described with Jones calculus, in which a matrix M represents the combined effects of the optical elements and the sample on the polarization state of the radiation [e.g. 15]:

$$\vec{E}^R = \begin{pmatrix} E_x^R \\ E_y^R \end{pmatrix} = M\vec{E}_I(\alpha), \tag{7}$$

where $\vec{E}_x^R$ and $\vec{E}_y^R$ are the x and y components of $\vec{E}^R$ and $\vec{E}_I$ is the light incident on the sample, see Fig. 1. α is the angle between the polarizer and the x-axis. The z-direction is chosen along the propagation direction of the light.

The experimental setup (Fig. 1) used here is based on reflection microscopy. For birefringence microscopy two relevant differences exist between transmission (as discussed in Refs. [9,10]) and reflection set-ups: (1) the ray path through the sample and (2) the presence of a beam splitter in the path of incident light, which leads to illumination with slightly elliptically polarized light.

First, the sample consists of a birefringent coating on top of a reflective metal, rather than just a birefringent layer. The Jones matrix of the sample is now given by:

$$\overbrace{M_{sample}^R}^{\text{Birefringent sample}} = \overbrace{M_r(\phi)M_s(\delta)M_r(-\phi)}^{\text{Birefringent coating}} \overbrace{M_m}^{\text{Metal substrate}} \overbrace{M_r(-\phi)M_s(\delta)M_r(\phi)}^{\text{Birefringent coating}}, \tag{8}$$

Taking M_m to represent a perfect mirror Eq. (8) can be rewritten as:

$$M^R_{\text{sample}} = M_m M_r(-\phi) M_s(2\delta) M_r(\phi). \tag{9}$$

For the intensity $I^R(\alpha)$ one finds:

$$I^R = E^R_x E^{R*}_x + E^R_y E^{R*}_y = \frac{I_I}{2}(1-|\sin 2\delta|\sin 2(\alpha+\phi)), \tag{10}$$

with I_I the intensity of the illumination reaching the sample. This is essentially equal to the expression shown in [9,10], the main difference being that 2δ appears because the light travels through the specimen twice.

Secondly, the beam splitter reflects light to the sample and transmits it to the CCD camera after interaction with the sample. The effect of the beam splitter on the polarization state and on the resulting intensity can be taken into account by modeling the reflection at the beam splitter as that from an aluminum mirror with surface normal at 45° with the propagation direction of the light, and neglecting transmission since the propagation direction of the rays is unaltered.

For the Jones matrix M_{bs} of the beam splitter one finds using Fresnel's formulae for reflection

$$M_{bs} = \begin{pmatrix} R_x & 0 \\ 0 & R_y \end{pmatrix} = \begin{pmatrix} \dfrac{n_2^2\sqrt{2n_2^2-1}-1}{n_2^2\sqrt{2n_2^2-1}+1} & 0 \\ 0 & \dfrac{1-\sqrt{2n_2^2-1}}{1+\sqrt{2n_2^2-1}} \end{pmatrix} \tag{11}$$
$$\cong \begin{pmatrix} 1 & 0 \\ 0 & -0.91-0.23i \end{pmatrix},$$

where R_x and R_y are the reflection coefficients (see Fig. 1), n_2 is the refractive index of Al, and where the refractive index of air has been taken equal to 1. Numerical values are given assuming $\lambda = 589.3$ nm and $n_2 = 1.44+5.23i$ [16]. Combining Eqs. (7), (8) and (8) results in:

$$\vec{E}_s = M_{cp} M_m M_r(-\phi) M_s(2\delta) M_r(\phi) \vec{E}_I, \tag{12}$$

where the incident radiation on the sample is now formulated as:

$$\vec{E}_I = M_{bs} \begin{pmatrix} E_0\cos\alpha \\ E_0\sin\alpha \end{pmatrix} = \begin{pmatrix} R_x E_0\cos\alpha \\ R_y E_0\sin\alpha \end{pmatrix}. \tag{13}$$

Here, E_0 is the amplitude of the illumination. Due to the imaginary reflection coefficients of the beam splitter the incident light becomes slightly elliptically polarized and the intensity of the light incident on the sample becomes a function of α:

$$I(\vec{E}_I) = R_x R^*_x E_0^2 \cos^2\alpha + R_y R^*_y E_0^2 \sin^2\alpha$$
$$= 0.875 E_0 \sin^2\alpha + 1.013 E_0 \cos^2\alpha. \tag{14}$$

The effect of varying illumination intensity and slight ellipticity on the determination of δ and ϕ was studied in the following way. A numerical experiment was performed in which the reflected intensity $I_s(\alpha)$ for several test-samples (each with unique values of δ and ϕ) was calculated, as well as the intensity $I_r(\alpha)$, the reflected intensity of a *reference* sample (a perfect mirror of the substrate material). Subsequently the hypothesis was tested that the slight ellipticity does not significantly interfere with the determination of δ and ϕ and that the intensity $I^N(\alpha)$ resulting from a simple normalization of $I_s(\alpha)$ by $I_r(\alpha)$:

$$I^N(\alpha) = \frac{I_s(\alpha)}{I_r(\alpha)}, \tag{15}$$

can serve as a base to determine δ and ϕ. Using a series of simulated $I_s(\alpha)$ and $I_r(\alpha)$, I_0, δ and ϕ were determined (using the procedure outlined in [9]) and compared to input values of the simulation. It was found that this procedure leads to a maximum error in δ of about 3% and of about 5% in ϕ. In view of other experimental uncertainties, these uncertainties are acceptable. In practice therefore an experimental reference series $I_r(\alpha)$ was measured with a mirror-like sample of the substrate material in addition to the series $I_s(\alpha)$ of the deformed layer that were determined for a number of strain levels. At each strain, the normalized intensity $I^N(\alpha)$ was used to determine I_0, δ and ϕ.

3. Experimental

The samples are coated with amorphous PET. The coatings were obtained by spin coating solutions of 2 wt.% and 4 wt.% PET in chloroform on polished dog-bone shaped specimens at 250 rpm, resulting in coating thicknesses of $L_0 = 4$ μm and $L_0 = 8$ μm respectively. After spin coating any excess of chloroform was removed by placing the specimen in a hot-air oven at 60 °C for 2 h. Prior to the measurements, the thickness was determined with a profilometer after locally removing the coating using a laser [17].

The measurements were performed with an in-situ uniaxial tensile stage at a constant speed of 5 μm/s. At predefined strains, the stage was halted and an image series $I_s(\alpha_i, u, v)$ was measured with $\alpha_i = 0, 15, \ldots, 345°$ and (u,v) the pixel location. The u direction is defined as the global tensile direction and is expressed as the horizontal axis in each of the following images. Prior to the measurements, a reference image series $I_r(\alpha_i,u,v)$ (see above) was obtained from an uncoated polished metal substrate.

The metal used was a stainless steel (19.5Cr1.8Mn8.8NiFe, determined by energy dispersive X-ray spectrometry) with an average grain size (determined by Electron Back Scatter Diffraction (EBSD)) of $d = 11.7$ μm.

Images of 1376 × 1032 pixels were taken with a 24-bit CCD camera. All $I_s(\alpha_i,u,v)$ are normalized using the reference series $I_r(\alpha_i, u, v)$. The actual determination of $|\sin 2\delta(u,v)|$, $\phi(u,v)$ and $I_0(u,v)$ from Eq. (10) was performed along the lines set out in Ref. [9]. The conversion from $|\sin 2\delta(u,v)|$ to $\Delta n(u,v)$ was performed with Eq. (6).

The green channel of the CCD was used ($\lambda = 510$ nm). Typical images are shown in Fig. 2.

4. Results and discussion

As mentioned in Section 1 our interest lies with the evolution of localized strains in the deformed PET layer. The results and

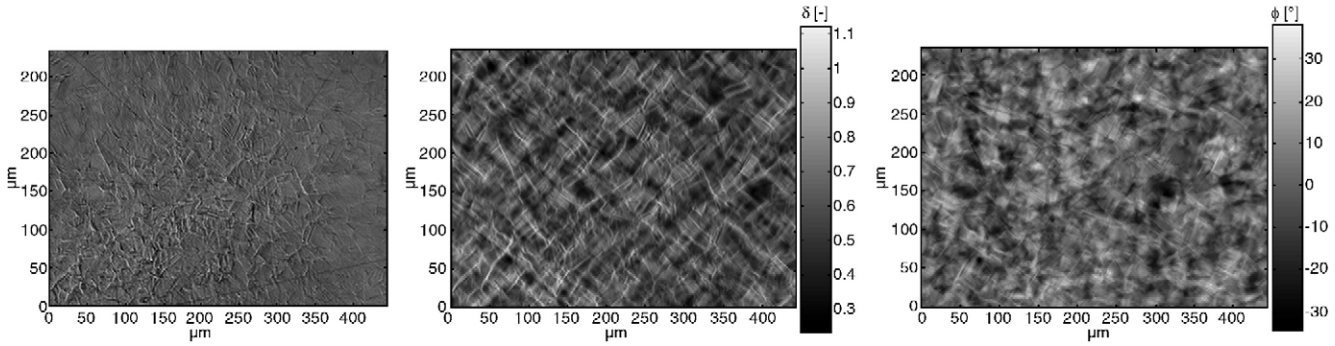

Fig. 2. Typical images of the intensity I_0 (left), phase factor δ and the extinction angle ϕ (right) of a coating with L_0=4 μm coating at ε=5%.

the discussion are organized in three parts: first the evolution of $\Delta n(\varepsilon)$ as a function of strain is discussed. This discussion entails the distribution of the measured values of $\Delta n(\varepsilon)$, the apparent stress-optical constant and strain-optical constants as well as the unwrapping technique employed. Secondly, spatial aspects of the evolution of $\Delta n(\varepsilon)$ are discussed, which leads to a discussion of the spatial correlation technique of measuring the evolution of $\Delta n(\varepsilon)$ at a fixed location in the material. In the discussion of the images spatial coordinates (u,v) will be used instead of (x,y) for clarity (see Fig. 1).

Fig. 3 shows $\Delta n(u,v)$ as a function of strain. For PET the global strain at yield is 4%–6% [3] so that at ε=2.5% PET is still expected to behave elastically. However, shear bands appear, indicating that locally PET is already plastically deforming. For increasing strains these shear bands become more pronounced. At a fixed strain ε the distribution of $\Delta n(\varepsilon)$ reflects the distribution of $|\varepsilon_2-\varepsilon_1|$ in the layer. Fig. 4 shows the evolution of the extremes of the distribution of $\Delta n(\varepsilon)$ as a function of ε. One point in the curves represents the average of either the 50 lowest ($\Delta n_{\min}(\varepsilon)$) or the 50 highest ($\Delta n_{\max}(\varepsilon)$) values of $\Delta n(\varepsilon)$ in the whole image. First, for low strains $\Delta n_{\min}(\varepsilon)$ as well as $\Delta n_{\max}(\varepsilon)$ increase linearly with strain. This is an indication that the distribution of stresses in the coating becomes wider as the strain increases. Second, a kink appears in both $\Delta n(\varepsilon)$ curves. For $\Delta n_{\min}(\varepsilon)$ it appears at ε=7.5% after which $\Delta n(\varepsilon)$ is constant, and or $\Delta n_{\max}(\varepsilon)$ it appears at ε=2.5% leading to a smaller slope.

The stress-optical constant C_{opt} can be determined from the following relationship:

$$\Delta n = C_{\text{opt}}(\sigma_{vv}-\sigma_{uu}) \quad \text{and at yield } \Delta n_Y = C_{\text{opt}}\sigma_Y, \tag{16}$$

where σ_Y is the yield stress. The yield stress of bulk PET is σ_Y=51 MPa [3], the stress-optical constant for a representative area becomes:

$$C_{\text{opt}} = \frac{\Delta n_Y}{\sigma_Y} \cong \frac{0.013}{51\text{MPa}} \cong (0.25\pm0.05)\text{GPa}^{-1}, \tag{17}$$

where the value at the kink in the curve of $\Delta n_{\max}(\varepsilon)$ in Fig. 4 is used to determine Δn_Y.

In Fig. 4 a second regime is visible starting at $\Delta n_Y \cong 0.013$. The amorphous PET used has a distinct softening behavior above yield [3]. During this phase, the global decrease in stresses involves an increase in the chain alignment. Therefore, Eq. (17) is limited to describe the stresses up to the strain at yield, which is taken at ε_Y=6%.

As inferred from theory, the orientation of the polymer is responsible for the changes in Δn. One can therefore define a strain-optical coefficient in both elastic and plastic regimes according to:

$$S_{\text{opt}}^{\text{elastic}} = \frac{\Delta n}{\varepsilon_{vv}-\varepsilon_{uu}} \cong \frac{\Delta n_Y}{\Delta \varepsilon_Y} \cong \frac{0.013}{0.06} \cong (0.22\pm0.05) \text{ and } S_{\text{opt}}^{\text{plastic}} \cong (0.10\pm0.02). \tag{18}$$

In literature several studies are devoted to the birefringence of drawn PET [18]. These studies focus on high draw ratios and

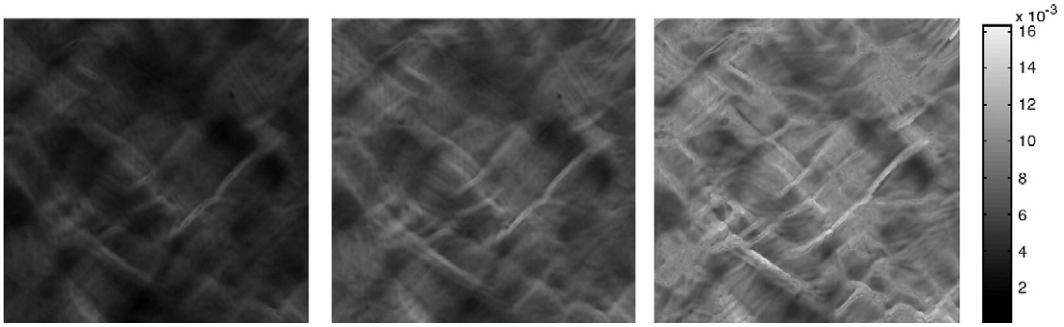

Fig. 3. $\Delta n(u,v)$ in an area of 97×97 μm^2 for increasing values of strain: ε=2.5% (left), 5% and 10% (right).

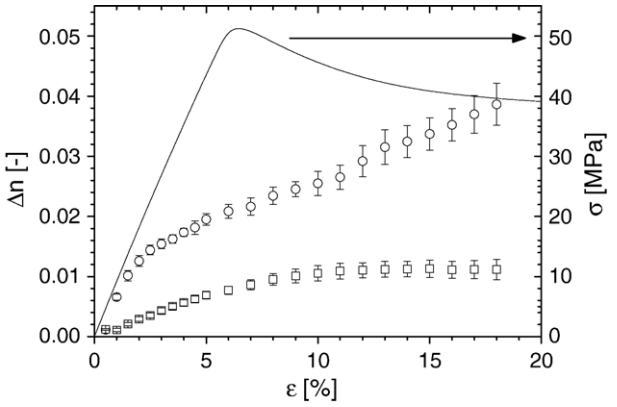

Fig. 4. Left axes: Δn as function of the global applied strain. ○: Δn averaged for 50 highest values and □: Δn averaged for 50 lowest values. Right axes: stress–strain curve of amorphous PET.

on temperatures above T_g. At 85 °C, the stress optical constant is $C_{opt} \approx 5.5\ GPa^{-1}$. Below T_g, this value is expected to drop rapidly [19]. No material for direct comparison with the low value encountered here is available.

In the following we discuss several aspects of the analysis.

4.1. Unwrapping

A relevant point of discussion is the unwrapping method that is applied to obtain a unique value of Δn. Since $|\sin 2\delta_\varepsilon(u,v)|$ in Eq. (10) is a periodic function, δ has no unique solution. In literature several unwrapping techniques have been proposed [10] usually based on a comparison of $|\sin 2\delta_\varepsilon(u,v)|$ or a number of different λ. The experiments discussed here offer an alternative method based on the deformation history at a certain material point (u_0,v_0).

Depending on the processing history there may be a small initial path difference $\delta_{\varepsilon=0}(u_0,v_0)=\delta_0$, but upon straining δ will start to increase as a function of ε. Upon measuring sufficient values of $|\sin 2\delta_\varepsilon(u,v)|$ and after converting them to $\delta_\varepsilon(u_0,v_0)$ a repetitive isosceles triangle function should appear for increasing ε (Fig. 5). Minima would appear at ε_{min} where $\delta_{\varepsilon_{min}}(u_0,v_0)=0$ and maxima at ε_{max} where $\delta_{\varepsilon_{max}}(u_0,v_0)=\pi/4$. At each extremum $\delta_\varepsilon(u_0,v_0)$ should be unwrapped for all strain values above the specific extremum strain, as sketched in the Fig. 5.

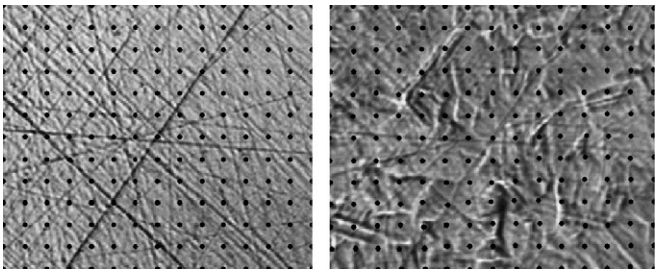

Fig. 6. Two correlated images of $I_0(u,v)(\varepsilon)$ for two different stages ($\varepsilon=0\%$ and 5%) of the coating with $L_0=4$ μm. The dots denote the correlated locations initially with a distance of 25 pixels (roughly 8 μm). Clearly visible is the deformation of the surface between both stages.

Importantly, in order to measure the evolution of $\delta_\varepsilon(u_0,v_0)$, the position $(u_0,v_0)(\varepsilon)$ has to be known as a function of strain. This is achieved using image correlation techniques on $I_0(u,v)(\varepsilon)$. The image correlation technique determine displacements between two sub-images of 32×32 pixels, which takes into account the fact that the deformation is inhomogeneous. A displacement vector is found for the point at the center of each sub-image. Combining the displacement vectors of the whole set of sub-images enables us to use interpolation techniques to find $(u_0,v_0)(\varepsilon)$. Fig. 6 shows a raster of correlated centre-points for two different stages of the straining process.

Fig. 7 shows the unwrapping in practice. One of the curves shows data (indicated by circles) representing the average of a random selection of 50 points from the specimen with $L_0=8$ μm. Clearly this curve starts to decrease at $\varepsilon=5\%$, and to increase again after about $\varepsilon=15\%$, indicating that unwrapping is necessary at these points. After unwrapping of each individual point in the underlying data set and redrawing the figure, a monotonically increasing relation between Δn and ε is found. In general, unwrapping becomes an important issue for thicker coatings or higher strains.

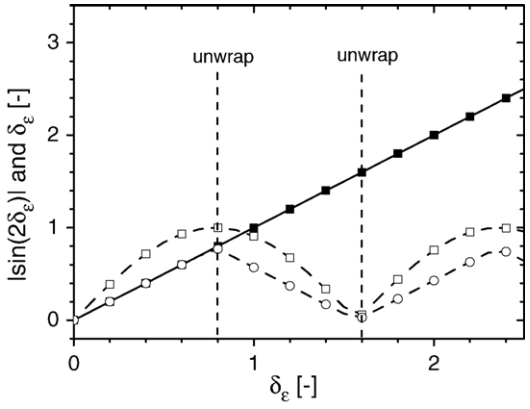

Fig. 5. The unwrapping process sketched: □: initial measurement, $|\sin(2\delta_\varepsilon)|$; ○: initial wrapped δ_ε; ■: true unwrapped δ_ε.

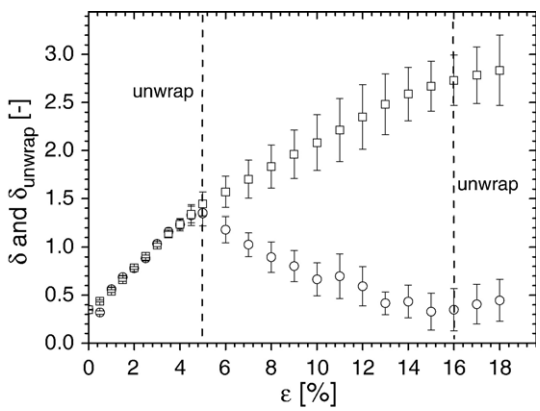

Fig. 7. Phase factor δ for the coating with $L_0=8$ μm averaged over 50 points in a shear band. □: with unwrapping, ○: without unwrapping.

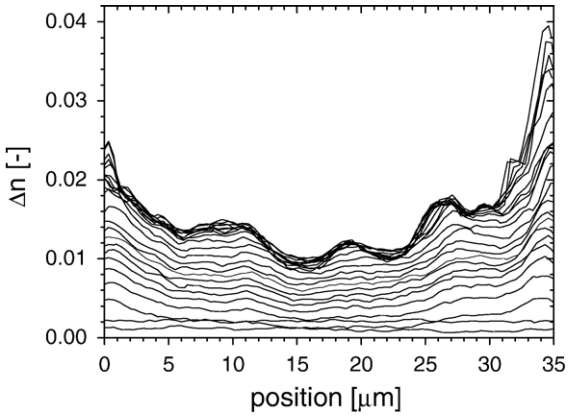

Fig. 8. Line profiles of Δn as a function of ε. The left- and right-hand sides of the lines correspond to the positions of two shear bands.

4.2. Spatial variations of Δn

To give an insight into the spatial variations in $\Delta n(\varepsilon)$ a set of line profiles is made between two shear bands at increasing values of ε. The left- and right-hand side of the lines in Fig. 8 correspond to locations of two shear bands. For increasing strains, the spacing between two subsequent lines in Fig. 8 changes. The spacing represents the increase in $\Delta n(\varepsilon)$ during the strain step.

It can be seen that there is a regime in which $\Delta n(\varepsilon)$ increases for all positions on the line when ε is increased. The increase is seen to be larger in the shear bands, and smaller in between the shear bands. Above a certain value of the strain, in the region in between the shear bands subsequent curves fall on top of each other, meaning that the increase in global strain no longer leads to a local change in the state of strain there. At the same time, it can be observed that the orientation in the shear bands keeps increasing, so the applied strain is concentrated there. It can be observed that close to the shear-bands, Δn doubles on a scale of a few microns.

The strain localization observed is caused by 1. the roughening of the interface and 2. the softening behavior of the amorphous PET.

At a macroscopic scale the softening behavior (shown in Fig. 4) leads to the formation of a neck when the material is deformed in tension. Material inside the neck is elongated until it starts to harden and material outside the neck remains elastic [20]. In the situation discussed here case the polymer cannot form a macroscopic neck and instead it forms a pattern of shear bands with elastically deformed regions in between. The curve representing the relaxed areas in Fig. 4 remains constant above $\varepsilon = 7.5\%$ at a level $\Delta n_c < \Delta n_Y$ indicating that they are indeed still elastic.

The fact that the shear bands show up before the macroscopic strain to yield is caused by the roughening of the steel substrate [6]. The rms roughness w of the surface of metals has been found to be a linearly increasing function of both grain size and strain for some metals (representing fcc, bcc and hcp crystal systems) without texture [e.g. 1,2].

In our case the stainless steel showed texture [6] and the dependence on grain size was not checked. The following function was found to describe the rms roughness w for this sample as a function of strain:

$$w = 1.4(1-e^{-3.4})\varepsilon \ (\mu\text{m}) \tag{19}$$

At the maximum strain of about 20% this amounts to an rms roughness of about 250 nm. Therefore, the coating thickness is always at least one order of magnitude larger than w.

The shear bands that originate at the interface may become wider and less intense as they stretch away from the interface [5,7]. Also, in the experiments, the value of Δn measured is actually an average across the thickness. Both effects mean that the variations in Δn measured in a thin layer (Fig. 9A) are more prominent than those measured in a thick layer (Fig. 9B).

5. Conclusions

From the characterization of PETG coated stainless steel with birefringence reflection microscopy the following conclusions are drawn: strain localization in PETG films supported by deforming metal films appears far below the strain at macroscopic yielding. The surface roughness of the substrate is the driving force for the localization. In thin coatings localization leads to the persistence of elastic regions at global strains above the yield strain. Thicker coatings show a diminishing contrast in the birefringence, due to averaging across

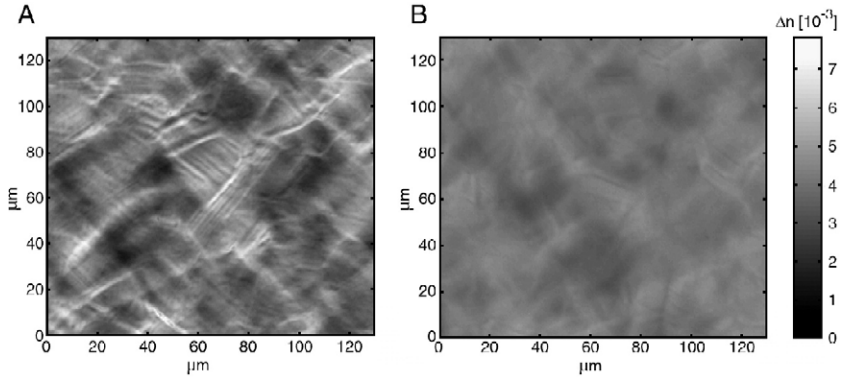

Fig. 9. Double refraction at $\varepsilon = 2.5\%$ for a coating of: A. 4 μm and B. 8 μm.

the thickness and widening of the shear bands away from the interface.

Acknowledgments

This work was financially supported by the STW (project number GTF.4901) and IOP (project number IOT 01001).

References

[1] O. Wouters, W.P. Vellinga, R. van Tijum, J.Th.M. De Hosson, Acta Mater. 53 (15) (2005) 4043.
[2] O. Wouters, W.P. Vellinga, R. van Tijum, J.Th.M. De Hosson, Acta Mater. 54 (2006) 2813.
[3] R. Rastogi. Aspects of plastic deformation of PET-steel laminates, PhD Thesis, University of Eindhoven (2003).
[4] W.P. Vellinga, R. Rastogi, H.E.H. Meijer, Proc. Mater. Res. Soc. 695 (2002) 21.
[5] R. van Tijum, W.P. Vellinga, J.Th.M. De Hosson, Adhesion on metal-polymer interfaces during plastic deformation, J. Mater. Sci. (in press).
[6] R. van Tijum, W.P. Vellinga, J.Th.M. De Hosson, in: R.E. Rudd, T.J. Balk, W. Windl, N. Bernstein (Eds.), Linking Length Scales in the Mechanical Behavior of Materials, MRS Proceedings, vol. 882E, 2005, p. EE3.2.
[7] R. van Tijum, W.P. Vellinga, J.Th.M. De Hosson, Surface roughening of metal-polymer systems during uniaxial plastic deformation, Acta Mater. (submitted for publication).
[8] R.H. Dauskardt, M. Lane, Q. Ma, N. Krishna, Eng. Fract. Mech. 61 (1) (1998) 141.
[9] A.M. Glazer, J.G. Lewis, W. Kaminsky, Proc. R. Soc. Lond., A Math. Phys. Sci. 452 (1996) 2751.
[10] A. Ajovalasit, S. Barone, G. Petrucci, J. Strain Anal. Eng. Des. 33 (2) (1998) 75.
[11] B.B. Doudou, E. Dargent, J. Grenet, J. Plast. Film Sheeting 21 (2005) 233.
[12] G.R. Strobl, The Physics of Polymers: Concepts for Understanding their Structures and Behavior, 2nd ed., Springer, 1997.
[13] M.A. O'Neill, R.A. Duckett, I.M. Ward, Polymer 29 (1988) 54.
[14] Y.S. Hu, V. Prattipati, A. Hiltner, E. Baer, S. Mehta, Polymer 46 (2005) 5202.
[15] M.A. Geday, W. Kaminsky, J.G. Lewis, A.M. Glazer, J. Microsc. 198 (1) (2000) 1.
[16] M. Born, E. Wolf, Principles of Optics, 7th (expanded) ed., Cambridge University Press, 1999.
[17] A. Fedorov, A. van Veen, R. van Tijum, J.Th.M. De Hosson, Proc. Mater. Res. Soc. 795 (2004) U8.61.
[18] R.G. Matthews, R.A. Duckett, I.M. Wald, D.P. Jones, Polymer 38 (19) (1997) 4795.
[19] J. Mulligan, M. Cakmak, Macromolecules 38 (2005) 2333.
[20] H.G.H. van Melick, L.E. Govaert, H.E.H. Meijer, Polymer 44 (2003) 3579.